Geometric origins of topological insulation in twisted layered semiconductors

Hao Tang, Stephen Carr, and Efthimios Kaxiras

Phys. Rev. B **104**, 155415 — Published 8 October 2021

DOI: 10.1103/PhysRevB.104.155415

Geometric origins of topological insulation in twisted layered semiconductors

Hao Tang,[1] Stephen Carr,[2] and Efthimios Kaxiras[3, 4]

[1] *Department of Physics, Peking University, Beijing, 100871, P.R.China*
[2] *Brown Theoretical Physics Center and Department of Physics, Brown University, Providence, Rhode Island 02912-1843, USA*
[3] *Department of Physics, Harvard University, Cambridge, Massachusetts 02138, USA*
[4] *John A. Paulson School of Engineering and Applied Sciences, Harvard University, Cambridge, Massachusetts 02138, USA*

(Dated: September 21, 2021)

Twisted bilayers of two-dimensional (2D) materials are proving a fertile ground for investigating strongly correlated electron phases. This is because the moiré pattern introduced by the relative twist between layers introduces long-wavelength effective potentials which lead to electron localization. Here, we develop a generalized continuum model for the electronic structure of moiré patterns, based on first-principles calculations and tailored to capture the physics of twisted bilayer 2D semiconductors. We apply this model to a database of eighteen 2D crystals covering a range of atomic relaxation and electronic structure features. Many of these materials host topologically insulating (TI) moiré bands in a certain range of twist angles, which originate from the competition between triangular and hexagonal moiré patterns, tuned by the twist angle. The topological phases occur in the same range as the maximally flat moiré bands.

I. INTRODUCTION

Quantum materials, engineered by creative manipulation of the features of conventional crystals, offer new possibilities for breakthroughs in understanding electron correlations and superconductivity. Often these phenomena emerge at a length scale much larger than the underlying crystal lattice constant (by a factor of 10 to 1000) due to strain-induced features. A recently popular platform for such studies are the few-layer two-dimensional (2D) crystals, like twisted bilayers of graphene or transition metal dichalcogenides (TMDCs) [1–5]. A slight lattice mismatch between two layers of a 2D material due to a a relative twist angle results in a moiré superlattice (MSL), introducing long-wavelength periodic modulation of the effective electronic potential [6, 7]. In a narrow range of the twist angle, the moiré potentials act as confining wells for the electrons of the constituent monolayers, causing isolated flat bands and localized wave functions near the Fermi surface [8, 9].

In the moiré flat bands, the kinetic energy is heavily suppressed and electronic interactions play a dominant role, with the intensity of the interactions controlled by the twist angle; this effect has been dubbed "twistronics" [10]. For example, the ultra flat band in polar 2D semiconductors are predicted in previous work [11–13]. Compared to twisted bilayer graphene (TBG), the twisted bilayer semiconductors can host flat bands in a large range of twist angles [14, 15] instead of at precisely a magic angle. This makes it possible to overcome some experimental challenges in twisted bilayers of semiconductors; thus, the twist angle becomes an additional degree of freedom for fine-tuning other physical effects in the strongly correlated regime [16]. Intriguingly, topological insulator (TI) moiré bands were predicted in twisted bilayer semiconductor systems [17–19], suggesting one could observe concurrent correlated and TI phases.

It is difficult to model twistronic systems at small twist angles ($\theta \leq 5^\circ$) using first-principles calculations because the number of atoms in the MSL scales as θ^{-2}. To overcome this limitation, continuum models with a low-energy effective Hamiltonian based on density functional theory (DFT) calculations were developed for electronic structures of TBG to accurately describe flat bands and magic angles [9, 20–22]. Although continuum models have also been applied to the twisted bilayer semiconductors [17, 23], they have yet to include the effect of atomic relaxations which play an important role at small angles [11, 14, 24, 25].

In this work, we present results from a DFT-based generalized continuum method designed specifically for twisted bilayer semiconductors. The computed electronic structures are consistent with full-DFT results [2, 11, 14] but only require a relatively inexpensive set of bilayer calculations. We derive a database of relevant physical parameters for describing the atomic relaxation and the electronic structure at band extremum for eighteen materials with various lattice symmetries and band edge momenta. Each layer contributes one band to the full twisted bilayer model, and these bands are coupled through a set of stacking-dependent electronic terms.

In Fig. 1 we provide an overview of the different phases and their geometric origins, as the twist angle is changed in a moiré bilayer (Fig. 1a). The full interaction between the bands can be decomposed into two complementary parts. The first describes the tendency for electrons in one layer to tunnel to the other, as shown in Fig. 1b – labeled Δ_T for "Tunneling". The tunneling coefficients are strongest at AA (aligned) stacking regions and form a triangular (TR) lattice across the MSL. The second contribution captures the stacking dependence of the monolayer bands' on-site energies, which depends on the electrostatic potential from the opposite layer, shown in Fig. 1c) – labeled Δ_t and Δ_b for "top/bottom" layer.

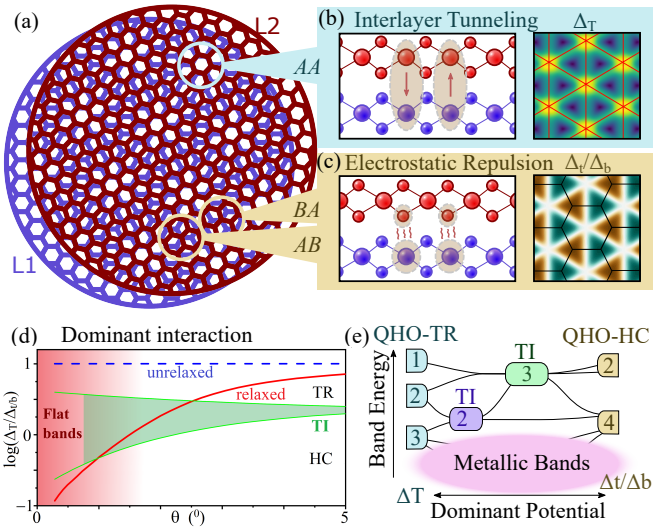

FIG. 1. (a) A moiré pattern of a twisted TMDC with areas of aligned (AA) stacking and eclipsed (AB or BA) stacking highlighted. (b) At AA stacking, the local electronic Hamiltonian is described by interlayer tunneling between the layers (Δ_T), forming a triangular (TR) lattice. (c) At AB or BA stacking, the electronic Hamiltonian is described by interlayer electrostatic potentials (Δ_t, Δ_b), forming a honeycomb (HC) lattice. (d) Twist-angle-dependent dominant moiré terms in TB WSe_2, with atomic relaxation of the superlattice (red line) or without it (blue line): evolution of the lattice character from TR to HC with *decreasing* θ induces TI states and flat bands at small angles. $\Delta_{T,t,b}$ in the vertical axis provides the potentials' leading order Fourier components. (e) Connectivity between the moiré bands. The TI phase is caused by band hybridization as the electrons transition between quantum harmonic oscillator (QHO) states on a TR to a HC lattice.

The electrostatic potentials have maxima at the AB and BA stacking regions, forming a honeycomb (HC) lattice.

In the majority of materials studied here, the in-plane atomic relaxation of the twisted bilayers enhances the effects of the electrostatic potential fluctuations and reduces that of the interlayer tunneling, especially at small twist angles. Electron localization transitions, from the tunneling-dominated TR lattice to the electrostatic-dominated HC lattice, occur at low twist angle in various materials, as illustrated in Fig. 1d. In the low-angle region, ultra-flat moiré bands are predicted, likely to host superconducting (SC) and Mott insulating (MI) phases. The topologically insulating (TI) moiré bands appear for intermediate values of the twist angle, during the transition between the two types of lattice geometries for the electronic terms (Fig. 1e). The electronic potentials naturally lead to quantum harmonic oscillator (QHO) states at small twist angles [26–28]. As electronic states localize at a specific stacking (either AA or AB/BA in TMDCs), the moiré potential can be expanded around the stacking center in a 2D harmonic form. Therefore, the energy levels of electrons (bands) become roughly identical to those of a 2D QHO. These localized QHO states explain the appearance of the moiré flat bands, their bandwidth is defined by the relative "leakage" between QHOs on neighboring moiré cells, and competition between different QHO stacking centers explains the large number of TI phases possible in twisted semiconductors.

II. METHODS

We here introduce the methodology for performing the atomic and electronic structure calculations within the continuum model. The translation symmetry of the moiré superlattice defines the moiré Brillouin zone (MBZ), as illustrated in Fig. 2a. The moiré bands closest to the band gap can be derived from the band extrema in the original Brillouin zone, which are typically located at high symmetry k-points. The local electronic structures are illustrated in Fig. 2b, where the bands of individual layers are shifted by the electrostatic potential $\Delta_{t,b}$ and split by the magnitude of the interlayer tunneling $2|\Delta_T|$.

To capture the stacking-dependent electronic and atomic details necessary for determination of the Δ potentials, we perform DFT calculations on aligned bilayers over a grid sampling the possible interlayer displacements. Using the effective mass approximation, we treat the dispersion around the monolayer band extrema as a kinetic energy term in a continuum Hamiltonian. Including the stacking-dependent Δ terms described above, we obtain the effective Hamiltonian:

$$H = \begin{pmatrix} -\frac{\hbar^2(\nabla - ik_0)^2}{2m^*} + \Delta_t(\boldsymbol{r}) & \Delta_T^*(\boldsymbol{r}) \\ \Delta_T(\boldsymbol{r}) & -\frac{\hbar^2(\nabla - ik_0)^2}{2m^*} + \Delta_b(\boldsymbol{r}) \end{pmatrix} \tag{1}$$

where m^* is the effective mass. We will see that such a two-band Hamiltonian at the K-edge of a semiconducting TMDC leads to topological phases.

To evaluate in-plane relaxation effects, we first minimize the total mechanical energy of the moiré patterns within a linear elastic plate model, using strain and stacking energies derived from DFT calculations [25]. Out-of-plane relaxation is implicitly included at the level of the DFT calculations, with each stacking allowed to move to its ideal interlayer separation. See the Supplementary Material (SM) [29] and the additional Refs. 30–34 included within for additional information. We incorporate the effect of atomic relaxations on the electronic Hamiltonian of Eq. (1) through a linear mapping starting from the unrelaxed configurations. As the stacking displacement is a function of the real space coordinate, $\boldsymbol{d}(\boldsymbol{r}) = \boldsymbol{\theta}\times\boldsymbol{r} + 2\boldsymbol{u}$, with $2\boldsymbol{u}$ the relative displacement from relaxation, the local band energy from DFT calculations can be expanded as

$$E^{(\pm)}(\boldsymbol{r}, \boldsymbol{k}) = E_m^{(\pm)}(\boldsymbol{d}(\boldsymbol{r})) + \frac{\hbar^2(\boldsymbol{k} - \boldsymbol{k}_0)^2}{2m^*} \tag{2}$$

with $E_m^{(\pm)}(\boldsymbol{d}(\boldsymbol{r}))$ the bonding (+) and antibonding (−) band extrema energy. The local band structure

$E^{(\pm)}(\boldsymbol{r},\boldsymbol{k})$ is well defined only when the moiré length scale is far larger than the unit cell, as required for the envelope function approximation [35]. To determine $\Delta_{t/b}, \Delta_T(\boldsymbol{r})$ from the local band energies, the layer polarization of the Bloch wave functions are extracted from the DFT calculations to assess how much of the variation in $E_m^{(\pm)}$ comes from band hybridization versus on-site potentials (see Fig. 2b and SM).

To calculate electronic properties of the twisted moiré bilayer, we implement a Hamiltonian $H(\boldsymbol{k})$ according to

$$H(\boldsymbol{k}) = \begin{pmatrix} \lambda_{\boldsymbol{k}} + \Delta_t(\boldsymbol{G}_u - \boldsymbol{G}_v) & \Delta_T^*(\boldsymbol{G}_u - \boldsymbol{G}_v) \\ \Delta_T(\boldsymbol{G}_u - \boldsymbol{G}_v) & \lambda_{\boldsymbol{k}} + \Delta_b(\boldsymbol{G}_u - \boldsymbol{G}_v) \end{pmatrix} \quad (3)$$

with $\lambda_{\boldsymbol{k}} = -\hbar^2(k - k_0 + G_u)^2\delta_{uv}/2m^*$ (a block-diagonal matrix with u, v as indices, and G_u as reciprocal lattice vectors) and $\Delta_i(\boldsymbol{G}_u - \boldsymbol{G}_v)$ representing scattering processes between low-energy states due to the twist angle. This matrix is diagonalized for a truncated set of moiré reciprocal $\boldsymbol{G}_m$ vectors, and requires only the Fourier coefficients of Δ_t, Δ_b, and Δ_T evaluated on moiré reciprocal lattice vectors.

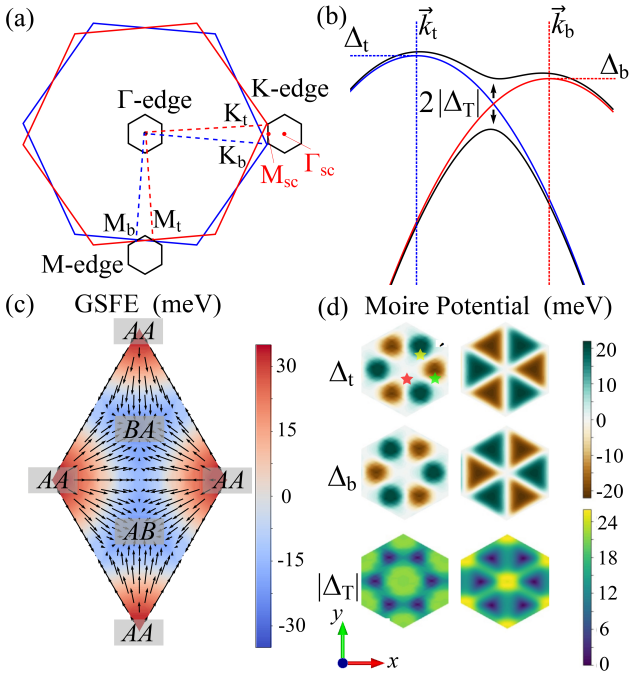

FIG. 2. Electronic model for the twisted bilayers. (a) Brillouin zones for a twisted bilayer of hexagonal lattices. The black hexagons show the MBZ expanded around selected high symmetry points. (b) Formation of moiré flat bands (black) from top (red) and bottom (blue) single-layer bands near the band extrema. (c) GSFE landscape (color) and atomic displacements (arrows) for a 2° twisted bilayer of WSe_2. (d) $\Delta t, b$ and $|\Delta_T|$ values from DFT without (left) and with (right) atomic relaxation; stars are placed adjacent to AA (red), AB (green), and BA (yellow) stacking.

III. RESULTS

A. Relaxation induced flat bands

The aligned (AA) stacking configuration has higher energy than the partially eclipsed (AB/BA) configuration for TMDCs and hBN homo-bilayers ($\theta \simeq 0°$). Consequently, relaxation tends to reduce the in-plane area of AA stacking region and to increase that of the AB/BA stacking region, thus minimizing the total energy (Fig. 2c) [21, 25]. Upon relaxation, the large values of $\Delta_{t,b}$, at AB and BA stacking, expand to cover a larger area, while the peak regions of Δ_T, at AA stacking, shrink (Fig. 2d). Therefore, the relaxed structures show stronger electrostatic potential effects and weaker tunneling effects, which causes a clear angle-dependent transition of the moiré electronic structure.

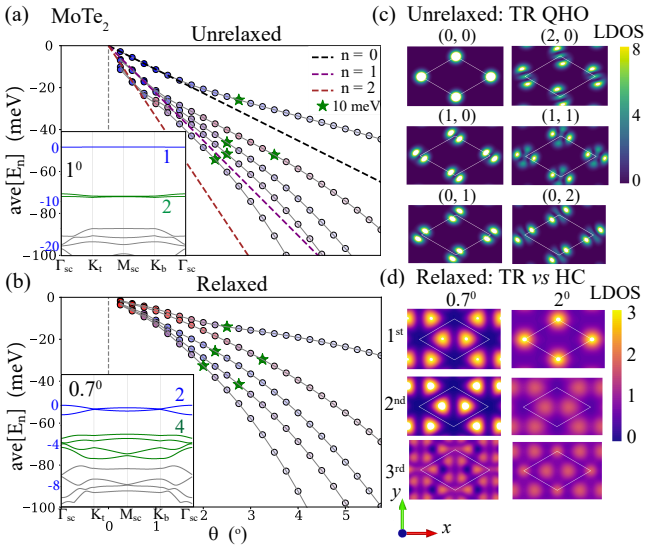

FIG. 3. Angle-dependent band structures and real-space localization. (a, b) The band average energy (ave[E_n], averaged over the MBZ), bandwidth (color saturation, deeper color for flatter bands), and localization (red for AB/BA stacking and blue for AA stacking) of the three top moiré valence bands as a function of the twist angle θ for twisted bilayers of 2H phase $MoTe_2$. A fitted QHO model is given by the dashed lines, and the first twist angles with bandwidths less than 10 meV are denoted with green stars. The 1/0.7° band structures are shown in the insets, with the first two QHO levels highlighted in color and the corresponding energy axis given in blue on the left. (c) LDOS of the top six moiré bands of unrelaxed bilayer $MoTe_2$ twisted at 0.5°. The quantum numbers in the QHO model are denoted as $n = (n_x, n_y)$. (d) LDOS of the moiré bands for a 0.7° and a 2° twisted bilayer of $MoTe_2$. The average LDOS in the MSL are normalized to one in both (c) and (d).

In Fig. 3a,b we present the angle-dependent bands and real-space localization of twisted bilayer $MoTe_2$ (2H phase) as a representative case. The top-most valence bands for both the relaxed and unrelaxed moiré systems

have a bandwidth less than 10 meV when the twist angle is below 2.5°. Using the Coulomb repulsion energy (U) in TBG and twisted hBN as a guide [4, 11], this small kinetic energy implies that strongly correlated states could exist for any twist angle below a certain critical value in some TMDC materials [2, 36]. The relaxation effects drive the small-angle ($< 2°$) valence moiré bands from TR-type to HC-type (Fig. 3). In the unrelaxed case, the band structure at 1° shows a single uppermost flat band and a pair of flat bands under it, consistent with a AA stacking QHO model, with energy levels $\hbar\omega(n_x + n_y + 1)$ [26, 27]. In contrast, a pair of top moiré bands and the four lower bands in the relaxed 0.7° structure correspond, respectively, to the first ($n = 0$) and second ($n = 1$) QHO states of the HC lattice [27].

The real space localization of the tunneling-dominated (TR) QHO state is evident in the local density of states (LDOS) of the moiré bands for the unrelaxed condition, as shown in Fig. 3c. The electronic states localize around the AA stacking center and show s, p, and d-orbital distribution for the first three energy levels, respectively. The six moiré bands shown correspond to the QHO ground state, single excitation states (2-fold degenerate), and double excitation states (3-fold degenerate). After relaxation, the competition between the two types of lattices is greatly altered, as shown in Fig. 3d. The two top bands in the low-angle case ($\theta = 0.7°$) localize in the AB/BA HC potential wells to from 2-fold degenerate ground states of the HC QHO model, while the third band is one of the 4-fold degenerate first excited states. As the twist angle increases, the localization of the uppermost band gradually changes to the AA stacking ($\theta = 2°$) with the second band localized in the AB/BA region. This indicates that the energy level of the HC QHO model and the triangular QHO model cross as the angle changes, leading to a reordering of the bands' localization. Therefore, the transition between the HC and TR electronic states can be controlled by varying the twist angle in the presence of atomic relaxations. The intermediate twist angles correspond to competing real-space distribution and band reordering, making these materials excellent candidates for hosting non-trivial topological properties.

B. Topological states

To study the topological properties associated with the TR-HC transition, we calculate the Chern numbers of the moiré bands from the +K valley for a generic twisted bilayer of a hexagonal semiconductor, and use these results to generate a TI phase diagram. The topological insulator phase ($Z_2 = 1$) refers to the quantum spin Hall insulator with opposite spin and non-zero Chern number at the ±K valley (under hole doping of 2 e/u.c.), and our discussion on topology does not cover the Γ-edge moiré bands [17]. The condition for the existence of topological bands is represented by the electrostatic potential

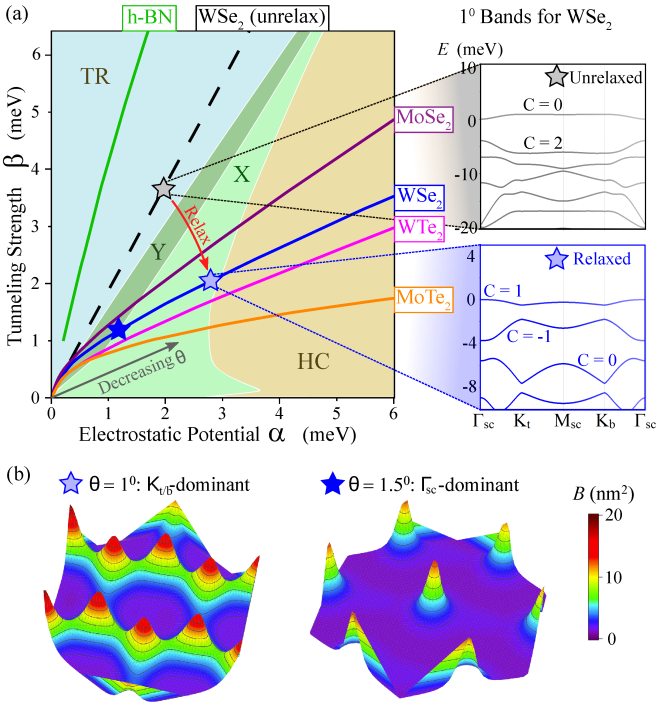

FIG. 4. Topological phase diagram for moiré bands. (a) Phase of the moiré bands as a function of the intensity of electrostatic potential α and tunneling fluctuations β (first Fourier components, defined in Eq.(4)). The light (dark) green areas represent X (Y) type TI phase, while the orange and light blue areas represent topologically trivial HC and TR QHO states, respectively. The twist-angle dependence of the relaxed band structures is shown by the solid lines for selected materials. The band structures and Chern numbers (C) for unrelaxed and relaxed moiré bands in 1° twisted bilayer WSe_2 are compared. (b) Berry curvature (B) of the uppermost band for X-type (1°) and Y-type (1.5°) twisted bilayer WSe_2 in the MBZ.

and tunneling coefficients in Fig. 4a for a generic system, which are approximated by their first order Fourier coefficients labeled V and w, respectively. In this simplified model, the topological properties can be completely described by just two parameters, the intensity of electrostatic potential $\alpha = Vm^*(a/a_0)^2/\theta^2$ and tunneling fluctuations $\beta = wm^*(a/a_0)^2/\theta^2$ (with $a_0 = 3.52$ Å, θ in degrees, and m^* in units of m_e), with the Hamiltonian

$$H \approx \hat{K} + \hat{V} + \hat{W} = \frac{\theta^2}{m^*(a/a_0)^2}\left(\hat{K_0} + \alpha\hat{V_0} + \beta\hat{W_0}\right) \quad (4)$$

where a is the lattice parameter, $\hat{K}$, $\hat{V}$, $\hat{W}$ are the kinetic, potential, and tunneling energy, respectively, and $\hat{K_0}$, $\hat{V_0}$, $\hat{W_0}$ are their material-independent counterparts. Using the first-order harmonic form of the V_0 and W_0 terms as an approximation, the topological properties can therefore be shown in a material-independent $\alpha - \beta$ phase diagram (Fig. 4a). The topologically trivial TR and HC phases appear in the w-dominated and V-dominated re-

gions of the phase space, respectively. Topologically non-trivial band structures occur in the intermediate region, and we focus on two situations for the top-most valence moiré bands. The Chern numbers of the three top-most moiré bands are observed to be either (1, -1, 0) and (1, 1, -2), which we label X-type and Y-type topological insulators, respectively. Transitions between topological and trivial insulators for the uppermost band will occur on the boundary between different phases.

In Fig. 4a we show the curves in the phase diagram of four 2H phase TMDCs, indicating transitions between phases with increasing twist angle (without relaxation these curves would be straight lines like the one shown for WSe_2). We mention that the 2H phase of ML WTe_2 in our calculation is a meta-stable phase [37], where the naturally occurring phase is 1T' [38]. For comparison, we include the curve for hBN, which remains in one phase (TR) as it exhibits weak relaxation in this twist angle range. An explicit example of the topological transitions is also shown Fig. 4a for WSe_2, including the unrelaxed case, which confirms that the topological transition is primarily driven by atomic relaxation.

In realistic experimental conditions, atomic-scale defects, bending, and local strain introduced during fabrication cause twisted bilayers to include different twist angles in different areas within a single sample [39]. Therefore, different domains of twist angle occur and introduce both topological and trivial bands. Topological edge states can appear along domain boundaries in the twist angle, according to the critical values in Tab. I. Therefore, the quantum spin Hall signature can be observed with spin-polarized edge current along the domain boundaries under magnetic field These edge states would not be defined by a sharp change from one crystal to another, or from material to vacuum, but rather by slow variation in the twist angle. For this reason, these "internal" protected edge states would be excellent candidates for observing spin or valley-polarized states, as the only disorder comes from twist-angle variations, which are unlikely to induce a spin or valley swapping.

TABLE I. $\theta_{\mathrm{HC/X}}, \theta_{\mathrm{X/Y}}$, and $\theta_{\mathrm{Y/TR}}$ are the critical twist angles (in degrees) for transitions of the top bands between the indicated phases. E_{gap} is the maximum band gap between the top and lower bands (in meV), and ω_{top} is the minimum band width of the top bands in the topologically non-trivial regime (in meV); θ_{gap} and θ_{top} are the angles where these extrema occur.

Material	$\theta_{\mathrm{HC/X}}$	$\theta_{\mathrm{X/Y}}$	$\theta_{\mathrm{Y/TR}}$	$E_{\mathrm{gap}}(\theta_{\mathrm{gap}})$	$\omega_{\mathrm{top}}(\theta_{\mathrm{top}})$
$MoSe_2$	0.9	1.4	2.4	2.98 (1.67°)	0.18 (1.21°)
$MoTe_2$	0.7	1.1	1.5	1.43 (1.20°)	0.30 (1.10°)
WSe_2	0.8	1.2	2.1	3.24 (1.40°)	0.19 (1.15°)
WTe_2	0.7	1.4	2.4	3.70 (1.68°)	0.18 (1.31°)

In Fig. 4b we show the Berry curvature of the uppermost valence band for two values of the twist angle. In the HC phase in the small-angle region, the first transition appears at $\theta_{\mathrm{HC/X}} = 1°$ where the two top bands separate at the MBZ's K points, indicated by the Berry curvature's concentration there. With increasing twist angle, the Berry curvature of the top band gradually transfers to the Γ point accompanied by an X/Y transition at $\theta_{\mathrm{X/Y}} = 1.5°$. At larger twist angle, the Berry curvature concentrates at the Γ point during the transition to the TR phase, where the two top-most bands merge. The numerical results for the critical angles, maximal gap, and minimal band width for the TMDCs with topological valence bands are presented in Table 1. We have also verified that the bands and real space localization of WSe_2 [2], and hBN [11] from our model are consistent with previous full DFT calculations.

Including spin degrees of freedom, the spin-dependent moiré Hamiltonian decomposes into two copies [17]. At the K valleys of the aligned bilayer, the two copies will be split by the spin-orbit coupling term, Δ_{SOC}, which for most TMDCs is on the scale of 100 meV, and the opposite spin-ordering will occur at the K' valley. The Γ and M points tend to have very weak spin-splitting, leading to two copies of the spin-independent Hamiltonian, as is the case in continuum treatments of twisted bilayer graphene [8]. However, as the two nonequivalent K valleys are related by time reversal symmetry, the spin-up bands at K valley and spin-down bands at K' valley have opposite Berry curvature and Chern numbers. Topologically non-trivial uppermost bands with opposite spin and Chern number give rise to the helical edge states protected by the TR symmetries at the boundaries, and could lead to observable quantum spin Hall (QSH) effects [40].

IV. CONCLUSION

The origin of the TI phases was previously ascribed [17] to a skyrmionic texture in the moiré Δ terms, which is an alternate interpretation of the TR/HC competition we presented here but captures the same key features. As the flatness of the bands causes stronger correlation effects, the topological phases in twisted bilayer semiconductors could exhibit the combination of TI and superconductivity, which has been the subject of an intense decades-long search for fractional statistics and Majorana fermions [40].

ACKNOWLEDGMENTS

We thank Ziyan Zhu, Daniel Larson, and Mattia Angeli for useful discussions. This work was supported by the National Science Foundation under grant No. OIA-1921199. The calculations in this work were performed in part on the FAS Research Computing cluster of Harvard University.

[1] Y. Cao, V. Fatemi, S. Fang, K. Watanabe, T. Taniguchi, E. Kaxiras, and P. Jarillo-Herrero, Unconventional superconductivity in magic-angle graphene superlattices, Nature **556**, 43 (2018).

[2] L. Wang, E.-M. Shih, A. Ghiotto, L. Xian, D. A. Rhodes, C. Tan, M. Claassen, D. M. Kennes, Y. Bai, B. Kim, *et al.*, Correlated electronic phases in twisted bilayer transition metal dichalcogenides, Nature Materials , 1 (2020).

[3] M. Yankowitz, S. Chen, H. Polshyn, Y. Zhang, K. Watanabe, T. Taniguchi, D. Graf, A. F. Young, and C. R. Dean, Tuning superconductivity in twisted bilayer graphene, Science **363**, 1059 (2019).

[4] Y. Cao, V. Fatemi, A. Demir, S. Fang, S. L. Tomarken, J. Y. Luo, J. D. Sanchez-Yamagishi, K. Watanabe, T. Taniguchi, E. Kaxiras, *et al.*, Correlated insulator behaviour at half-filling in magic-angle graphene superlattices, Nature **556**, 80 (2018).

[5] U. Zondiner, A. Rozen, D. Rodan-Legrain, Y. Cao, R. Queiroz, T. Taniguchi, K. Watanabe, Y. Oreg, F. von Oppen, A. Stern, *et al.*, Cascade of phase transitions and dirac revivals in magic-angle graphene, Nature **582**, 203 (2020).

[6] J. M. B. Lopes dos Santos, N. M. R. Peres, and A. H. Castro Neto, Graphene bilayer with a twist: Electronic structure, Phys. Rev. Lett. **99**, 256802 (2007).

[7] C.-H. Park, L. Yang, Y.-W. Son, M. L. Cohen, and S. G. Louie, Anisotropic behaviours of massless dirac fermions in graphene under periodic potentials, Nature Physics **4**, 213 (2008).

[8] R. Bistritzer and A. H. MacDonald, Moiré bands in twisted double-layer graphene, Proceedings of the National Academy of Sciences **108**, 12233 (2011).

[9] E. S. Morell, J. Correa, P. Vargas, M. Pacheco, and Z. Barticevic, Flat bands in slightly twisted bilayer graphene: Tight-binding calculations, Physical Review B **82**, 121407 (2010).

[10] S. Carr, D. Massatt, S. Fang, P. Cazeaux, M. Luskin, and E. Kaxiras, Twistronics: Manipulating the electronic properties of two-dimensional layered structures through their twist angle, Phys. Rev. B **95**, 075420 (2017).

[11] L. Xian, D. M. Kennes, N. Tancogne-Dejean, M. Altarelli, and A. Rubio, Multiflat bands and strong correlations in twisted bilayer boron nitride: Doping-induced correlated insulator and superconductor, Nano Letters **19**, 4934 (2019).

[12] N. R. Walet and F. Guinea, Flat bands, strains, and charge distribution in twisted bilayer $h-$BN, Phys. Rev. B **103**, 125427 (2021).

[13] X.-J. Zhao, Y. Yang, D.-B. Zhang, and S.-H. Wei, Flat bands in twisted bilayers of polar two-dimensional semiconductors, Phys. Rev. Materials **5**, 014007 (2021).

[14] M. H. Naik and M. Jain, Ultraflatbands and shear solitons in moiré patterns of twisted bilayer transition metal dichalcogenides, Physical review letters **121**, 266401 (2018).

[15] X.-J. Zhao, Y. Yang, D.-B. Zhang, and S.-H. Wei, Formation of bloch flat bands in polar twisted bilayers without magic angles, Phys. Rev. Lett. **124**, 086401 (2020).

[16] A. Kerelsky, L. McGilly, D. M. Kennes, L. Xian, M. Yankowitz, S. Chen, K. Watanabe, T. Taniguchi, J. Hone, C. Dean, *et al.*, Magic angle spectroscopy, arXiv preprint arXiv:1812.08776 (2018).

[17] F. Wu, T. Lovorn, E. Tutuc, I. Martin, and A. MacDonald, Topological insulators in twisted transition metal dichalcogenide homobilayers, Physical review letters **122**, 086402 (2019).

[18] H. Pan, F. Wu, and S. Das Sarma, Band topology, hubbard model, heisenberg model, and dzyaloshinskii-moriya interaction in twisted bilayer wse_2, Phys. Rev. Research **2**, 033087 (2020).

[19] S. Javvaji, J.-H. Sun, and J. Jung, Topological flat bands without magic angles in massive twisted bilayer graphenes, Phys. Rev. B **101**, 125411 (2020).

[20] S. Carr, S. Fang, Z. Zhu, and E. Kaxiras, Exact continuum model for low-energy electronic states of twisted bilayer graphene, Physical Review Research **1**, 013001 (2019).

[21] J. Jung, A. Raoux, Z. Qiao, and A. H. MacDonald, Ab initio theory of moiré superlattice bands in layered two-dimensional materials, Physical Review B **89**, 205414 (2014).

[22] S. Fang and E. Kaxiras, Electronic structure theory of weakly interacting bilayers, Physical Review B **93**, 235153 (2016).

[23] F. Wu, T. Lovorn, E. Tutuc, and A. H. MacDonald, Hubbard model physics in transition metal dichalcogenide moiré bands, Physical review letters **121**, 026402 (2018).

[24] N. N. T. Nam and M. Koshino, Lattice relaxation and energy band modulation in twisted bilayer graphene, Phys. Rev. B **96**, 075311 (2017).

[25] S. Carr, D. Massatt, S. B. Torrisi, P. Cazeaux, M. Luskin, and E. Kaxiras, Relaxation and domain formation in incommensurate two-dimensional heterostructures, Physical Review B **98**, 224102 (2018).

[26] S. Carr, D. Massatt, M. Luskin, and E. Kaxiras, Duality between atomic configurations and bloch states in twistronic materials, Phys. Rev. Research **2**, 033162 (2020).

[27] M. Angeli and A. H. MacDonald, Γ-Valley Transition-Metal-Dichalcogenide Moirè Bands, arXiv e-prints , arXiv:2008.01735 (2020), arXiv:2008.01735 [cond-mat.str-el].

[28] M. H. Naik, S. Kundu, I. Maity, and M. Jain, Origin and evolution of ultraflat bands in twisted bilayer transition metal dichalcogenides: Realization of triangular quantum dots, Phys. Rev. B **102**, 075413 (2020).

[29] See Supplemental Material at [URL] for additional details on the DFT calculations and analysis of band topology.

[30] G. Kresse and J. Furthmüller, Efficient iterative schemes for ab initio total-energy calculations using a plane-wave basis set, Phys. Rev. B **54**, 11169 (1996).

[31] G. Kresse and D. Joubert, From ultrasoft pseudopotentials to the projector augmented-wave method, Phys. Rev. B **59**, 1758 (1999).

[32] J. Sun, A. Ruzsinszky, and J. P. Perdew, Strongly constrained and appropriately normed semilocal density functional, Phys. Rev. Lett. **115**, 036402 (2015).

[33] J. Sun, R. C. Remsing, Y. Zhang, Z. Sun, A. Ruzsinszky, H. Peng, Z. Yang, A. Paul, U. Waghmare, X. Wu, *et al.*, Accurate first-principles structures and energies of

diversely bonded systems from an efficient density functional, Nature chemistry **8**, 831 (2016).
[34] H. Peng, Z.-H. Yang, J. P. Perdew, and J. Sun, Versatile van der waals density functional based on a meta-generalized gradient approximation, Phys. Rev. X **6**, 041005 (2016).
[35] B. A. Foreman, Envelope-function formalism for electrons in abrupt heterostructures with material-dependent basis functions, Phys. Rev. B **54**, 1909 (1996).
[36] Z. Zhang, Y. Wang, K. Watanabe, T. Taniguchi, K. Ueno, E. Tutuc, and B. J. LeRoy, Flat bands in twisted bilayer transition metal dichalcogenides, Nature Physics 10.1038/s41567-020-0958-x (2020).
[37] N. Mounet, M. Gibertini, P. Schwaller, D. Campi, A. Merkys, A. Marrazzo, T. Sohier, I. E. Castelli, A. Cepellotti, G. Pizzi, *et al.*, Two-dimensional materials from high-throughput computational exfoliation of experimentally known compounds, Nature nanotechnology **13**, 246 (2018).
[38] C. Lee, E. Silva, and L. e. a. Calderin, Tungsten ditelluride: a layered semimetal, Sci Rep **5**, 10013 (2015).
[39] A. Uri, S. Grover, Y. Cao, J. A. Crosse, K. Bagani, D. Rodan-Legrain, Y. Myasoedov, K. Watanabe, T. Taniguchi, P. Moon, M. Koshino, P. Jarillo-Herrero, and E. Zeldov, Mapping the twist-angle disorder and landau levels in magic-angle graphene, Nature **581**, 47 (2020).
[40] X.-L. Qi and S.-C. Zhang, Topological insulators and superconductors, Rev. Mod. Phys. **83**, 1057 (2011).